Na_xCoO_2 phase stability and hierarchical orderings in the O3/P3 structure family

Jonas L. Kaufman and Anton Van der Ven*
Materials Department, University of California, Santa Barbara, Santa Barbara, California 93106, USA

(Received 10 August 2018; revised manuscript received 7 November 2018; published 10 January 2019)

The operation of Na-ion batteries is closely linked to the occurrence of phase transitions and Na ordering within the electroactive materials of their electrodes. We performed a first-principles study of Na_xCoO_2 ($0 \leqslant x \leqslant 1$) to establish phase stability among O3, P3, O1, and staged hybrid O1-O3 host structures and to determine low-energy Na orderings within each host. We predict several staircases of ground-state orderings, many of which are found to remain ordered at room temperature. At high Na content, the ground states belong to a family of vacancy row orderings in O3 with distorted CoO_2 layers. In P3, where the available Na sites form a honeycomb network, we discover three families of hierarchical ground-state orderings at intermediate compositions that essentially consist of domains of the $x = 1/2$ ground state periodically separated by antiphase boundaries. Our results agree with the experimentally reported voltage profile and the observed changes in stacking sequence with Na concentration.

DOI: 10.1103/PhysRevMaterials.3.015402

I. INTRODUCTION

Na-ion batteries offer a promising alternative to Li-ion batteries for applications in which weight is not critical. Layered intercalation compounds have received widespread attention as positive electrodes for both technologies since the 1980s [1–3]. Layered Na intercalation compounds typically undergo more structural phase transformations upon cycling compared to their Li counterparts [4–21] due to the stability of both octahedral and prismatic Na coordination [22,23]. Furthermore, host structures that offer prismatic sites to Na allow for more complex Na-vacancy orderings than are possible in hosts with octahedral sites. Structural phase transitions and Na orderings are both important in determining the voltage profile, susceptibility to degradation, and diffusion mechanisms of electrode materials.

Many layered transition-metal oxide and sulfide Na intercalation compounds have been investigated experimentally [2] and computationally [24–27]. Two distinct types of phases are synthesized: P2 and O3, with the latter converting to P3 upon deintercalation through the gliding of transition-metal oxide/sulfide slabs. O3-type Na_xCoO_2 ($0 \leqslant x \leqslant 1$) is among the oldest [28] and most studied layered Na intercalation compounds [2], but the details of Na ordering as the compound is deintercalated are not well understood. Experimental voltage profiles suggest rich ordering phenomena in the P3 phase for intermediate Na content, but so far no comprehensive picture of these orderings has been established.

An overview of the O3-type Na_xCoO_2 host structures considered in this study is shown in Fig. 1. Each consists of stacked triangular lattices of O alternated by layers of Co and Na/vacancies. The Co and O layers form sheets of edge-sharing CoO_6 octahedra, and the stacking sequence of the O layers determines the coordination of the Na sites. In O1 stacking (AB), each Na site is octahedrally coordinated by O and shares faces with the two neighboring CoO_6 octahedra. In O3 stacking (AB CA BC), the Na sites are also octahedrally coordinated but do not share faces with CoO_6 octahedra. In P3 stacking (AB BC CA), each Na site is prismatically coordinated and shares a face with a single CoO_6 octahedron, either above or below. While the Na sites in O1 and O3 belong to a single triangular lattice, those in P3 lie on one of two distinct triangular lattices that together form a honeycomb network. This allows for Na-Na pair distances in P3 that are not available in O1 or O3, expanding the possible orderings that Na may take on to minimize electrostatic interactions [26]. Phase transformations within this set of structures are accomplished by gliding of CoO_2 sheets, without the need to break strong bonds. In addition to the pure structures O1, O3, and P3, hybrid structures such as O1-O3 (also known as H1-3) and O1-P3 are also possible. The labels O′3 or P′3 are commonly used to indicate a distortion of the O3 or P3 parent structure [28].

In this study, we use first-principles techniques to predict phase stability and ground-state Na orderings within the various host structures that can be derived from O3-type Na_xCoO_2 through a simple shearing of the CoO_2 sheets. P3 is found to be stable at intermediate compositions, in agreement with experiment, as well as O3 and a hybrid O1-O3 phase at lower compositions. We identify several families of hierarchical orderings in O3 and P3 that result in staircases of stable periodic ground states. These are predicted to remain ordered at room temperature and together produce a sloping voltage profile consisting of many small steps and plateaus similar to that observed experimentally. We find that the zigzag row motif found at $x = 1/2$ forms the basis of all ground-state orderings in P3 Na_xCoO_2. We discuss the likelihood of the same orderings appearing in other layered intercalation compounds.

II. METHODS

Density functional theory (DFT) calculations were performed with the Vienna *ab initio* Simulation Package (VASP)

*avdv@ucsb.edu

 ©2019 American Physical Society

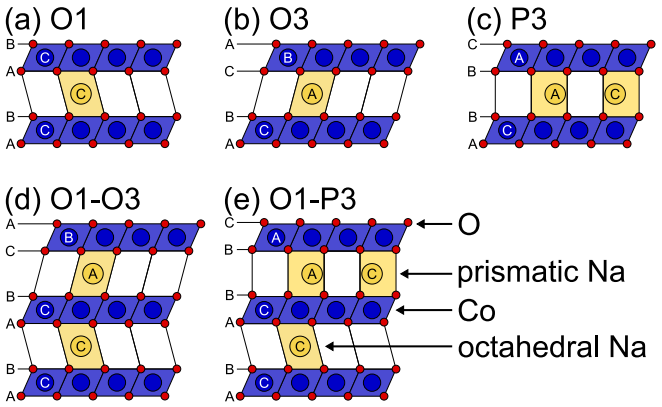

FIG. 1. Stacking sequences of the (a) O1, (b) O3, and (c) P3 structures and the hybrid structures (d) O1-O3 and (e) O1-P3. Polyhedra are shown as parallelograms with O (red circles) at the corners. Co (blue circles) occupy octahedral sites while Na (yellow circles) occupy either octahedral sites on a single triangular sublattice or prismatic sites on two distinct triangular sublattices.

[29–32]. The projector augmented wave (PAW) method [33,34] was used with a plane-wave energy cutoff of 700 eV. The optB86b-vdW exchange-correlation functional [35] was used to account for van der Waals interactions, which are necessary to accurately describe the interlayer cohesion near complete deintercalation [36,37]. The Brillouin zone was sampled using Γ-centered Monkhorst-Pack meshes [38] with a density of 38 Å along each reciprocal lattice vector. All calculations were spin polarized, with ferromagnetic ordering assumed. A quasi-Newton algorithm was used for ionic relaxations, as well as Gaussian smearing with a width of 0.1 eV. Forces were converged within to 0.02 eV/Å. To obtain accurate final energies, all relaxations were followed by a final static calculation with the linear tetrahedron method [39].

Although the addition of a Hubbard U correction can produce average voltages in better agreement with experiments [37], this method was not used because it has been shown to yield some unphysical results in layered cobalt oxide systems. Specifically, a typical U value of 3 eV or greater inverts the phase stability between O1 and O3 in CoO_2 [37] and leads to incorrect ordering tendencies in P2-Na_xCoO_2 [40]. DFT without U, conversely, has been used to accurately predict phase stability in Li_xCoO_2 [41,42]. A hybrid functional such as Heyd-Scuseria-Ernzerhof (HSE) was not used in this study due to the computational cost, inability to capture van der Waals effects in CoO_2 [43], and demonstrated overprediction of voltages in Li_xCoO_2 [37,43].

The Clusters Approach to Statistical Mechanics (CASM) software package [44–47] was used to enumerate symmetrically distinct configurations within each host structure across the composition range of Na_xCoO_2. DFT energies were calculated for 22 O1 configurations, 339 O3 configurations, 365 P3 configurations, 34 O1-O3 configurations, and 60 O1-P3 configurations. For hybrid structures, only those configurations containing zero Na in the O1 layers were enumerated because O1 was found to be unstable for $x > 0$, in agreement with previous studies [26,48]. Cluster expansion effective Hamiltonians were fit for each host structure (except O1) and used iteratively to predict new near-ground-state configurations for which to calculate DFT energies. The cluster expansions made it feasible to traverse the configuration space at large supercell volumes. Monte Carlo heating and cooling runs were performed for a grid of temperatures and chemical potentials. For further details of the cluster expansions and Monte Carlo simulations, we refer the reader to the Supplemental Material [49]. Free energy integration of our Monte Carlo results showed that at room temperature (300 K), the ordered ground states are more stable than the disordered phases resulting from cooling runs and that the ground states do not disorder appreciably until above 400 K. For this reason, all phases were treated as line compounds, i.e., the free energies at room temperature were taken to be the zero-temperature formation energies obtained from DFT. Unless otherwise noted, all reported energies and structures are DFT predictions.

The cathode voltage is related to the Na chemical potential μ_{Na} by

$$V = -\frac{\mu_{Na} - \mu^{\circ}_{Na}}{e}, \tag{1}$$

where μ°_{Na} is the Na chemical potential in the reference anode and e is the elementary charge. Hexagonal close-packed Na metal was chosen as the reference.

III. RESULTS

A. Phase stability

Figure 2(a) shows the calculated formation energies and the convex hull for each host structure. As reference states, we use O1 CoO_2 and O3 $NaCoO_2$. The global convex hull is outlined in black. O1 is predicted to be globally stable only at $x = 0$ and is not shown for other compositions. O3 is globally stable both for $1/3 \leqslant x \leqslant 3/8$ and $4/5 \leqslant x \leqslant 1$, while P3 is stable for intermediate Na concentration, $5/11 \leqslant x \leqslant 2/3$. The width of the two-phase region between O3 at $x = 3/8$ and P3 at $x = 5/11$ may be smaller than is shown, as there are several P3 ground states in this region that are above the global convex hull by less than 1 meV/CoO_2, which is well within numerical error of the DFT calculations. For the hybrid structures, O1-P3 is not found to be globally stable, while O1-O3 is stable at $x = 1/6$. The predicted phase stability agrees with experimental studies by Lei *et al.* [9] and Kubota *et al.* [50] for $x \geqslant 1/2$. The characterization of structure for lower compositions has proven difficult experimentally [50], so we cannot compare our results for $x < 1/2$ as closely.

The slope of the formation energy is related to the chemical potential of Na, which is used to calculate the equilibrium voltage curve in Fig. 2(b). Each plateau corresponds to a two-phase region, while each step corresponds to a ground-state ordering. We have identified four families of hierarchical ground-state orderings, whose predicted composition ranges are indicated in Fig. 2(b) along with important orderings at their endpoints. The ζ^- and ζ^+ orderings in P3 can be generated by combining translational variants of the $x = 1/2$ ground-state ordering (ζ) separated by antiphase boundaries (APBs). Similarly, the η^+ orderings can be generated from the orientational variants of the $x = 4/7$ ground state (η) separated by APBs. The θ orderings in O3 consist of fully sodiated regions separated by rows of vacancies. We will

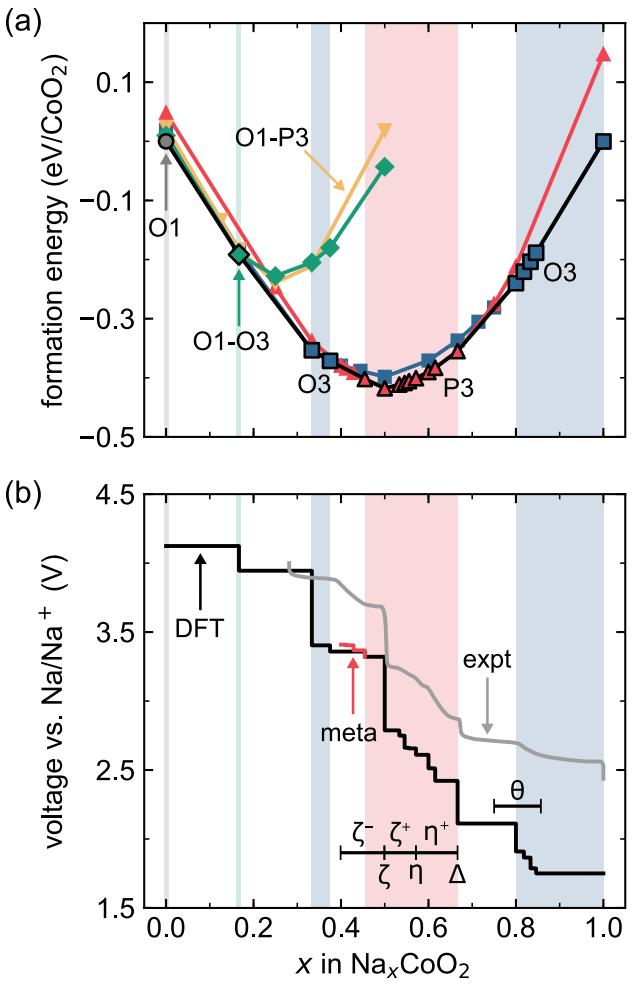

FIG. 2. (a) Calculated formation energies vs composition for configurations on the local convex hull of each host structure. The global convex hull is shown in black. Single phase regions are highlighted in the background. (b) Calculated zero-temperature equilibrium voltage curve (black) compared to experiment from Kubota *et al.* [50] (gray). A section of the metastable P3 voltage curve is shown in red. The composition ranges for various families of orderings in P3 and O3 are indicated.

examine these families of orderings in detail along with the other ground states.

The calculated equilibrium voltage curve in Fig. 2(b) is compared to the experimental curve from Kubota *et al.* [50]. The relative jaggedness of the calculated curve is in part due to a finite sampling of the large number of possible orderings in each family of ground states. Our voltage underpredicts experiment by about 0.5 V, which is consistent with systematic errors inherent to approximations to DFT when comparing energies of metals and oxides. The voltage of the O3 region for $x \geqslant 4/5$ is predicted to be lower still. We attribute this underprediction to an inability of DFT approaches in accurately describing charge localization in the vicinity of the metal-insulator transition in cobalt oxide compounds at high intercalant concentrations [41]. Despite these issues, the overall qualitative agreement with experiment is good.

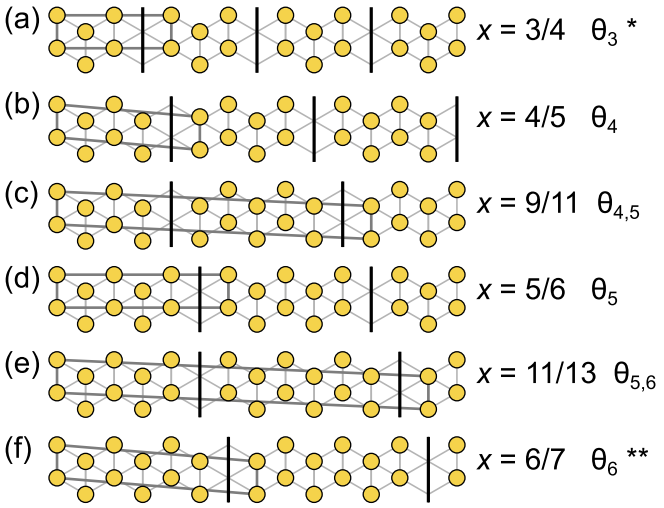

FIG. 3. Orderings belonging to the θ family on the local convex hull of O3. Yellow circles represent Na and black lines indicate vacancy rows between fully sodiated regions. Unit cells are shown in dark gray. Single asterisks indicate that the ordering is above the global hull and double asterisks indicate that the ordering is also above the local hull but by less than 0.5 meV/CoO_2.

We predict a large step of about 0.5 V at $x = 1/2$ and a smaller one at $x = 2/3$, with a sloping region rich in small steps and plateaus between the steps at $x = 1/2$ and 2/3. The metastable P3 voltage curve corresponding to the ζ^- family of orderings is shown in red and may be the path followed experimentally as the equilibrium path requires a two-phase reaction from P3 to O3.

B. O3 orderings

At $x = 1$, there is only one ordering possible in O3 as all Na sites are then filled. For $3/4 \leqslant x \leqslant 6/7$, we find that the O3 ground states all consist of different arrangements of rows of vacancies as shown in Fig. 3. There are an infinite number of orderings in this family with different sequences of spacings between vacant rows, resulting in a "devil's staircase" [51,52] of stable ground states at almost arbitrary composition. We refer to this family of orderings as θ and present a naming convention and composition formula for specific orderings in the Appendix 1.

The θ orderings bring about significant distortions of the O3 host, as shown in Fig. 4. Na directly adjacent to the vacancy rows are displaced from the centers of their octahedral sites toward the vacancies, and the interlayer spacing tends to expand around the vacancies, resulting in undulating CoO_2 layers. Configurations in which vacancy rows are not stacked immediately on top of each other seem to be energetically preferred, though we did not probe this exhaustively. The strong distortions made it difficult to parametrize an accurate cluster expansion, so we were unable to perform reliable Monte Carlo simulations to determine if the θ orderings remain ordered at room temperature. We expect, however, that the rows are "locked in" such that breaking them is energetically unfavorable. To test this, we calculated the energies of perturbed structures in which every fourth Na in a row adjacent to a

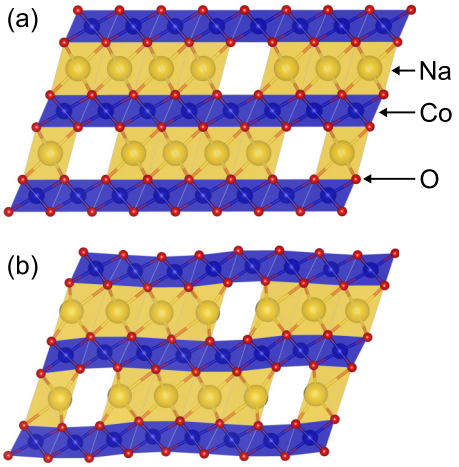

FIG. 4. Structure of the θ_4 ground state at $x = 4/5$ (a) before and (b) after relaxation. Visualization created using VESTA [53].

vacant row was moved into the vacant row itself. This was found to increase the energy by 283 and 384 meV for θ_3 and θ_4 [Figs. 3(a) and 3(b)], respectively. These are large energy increases, and we therefore expect that the θ ground states will remain ordered at room temperature.

Experimental studies report a stable O′3 phase, described as O3 with a monoclinic distortion, from $x = 0.8$ or 0.83 to around 0.86 or 0.88, followed by a two-phase region between O′3 and hexagonal O3 at $x = 1$ [9,50]. This composition range is similar to that where the θ family is found to be stable. The predicted two-phase region between fully sodiated O3 and $\theta_{5,6}$ at $x = 11/13$ coincides with the experimental two-phase region. Other θ orderings having Na concentrations that are slightly higher than $x = 11/13$, such as θ_6, θ_7, and θ_8, were predicted to be only 1–2 meV/CoO_2 above the global convex hull.

As is evident in Fig. 2(a), the O3 host is not only stable at high Na concentrations but also at concentrations around $x = 1/3$. Figure 5 shows ground-state orderings in O3 for $1/3 \leqslant x \leqslant 1/2$. The $x = 1/3$ ordering in Fig. 5(a) is the typical $\sqrt{3}a \times \sqrt{3}a$ ordering on a triangular lattice, where a is the lattice parameter. The orderings at $x = 3/8$ and $x = 2/5$ [Figs. 5(b) and 5(c)] can be viewed as consisting of different translational variants of the $x = 1/3$ ordering separated by APBs. This suggests that there could be another family of O3 ground-state orderings in this composition range with different spacings of APBs, but we have not pursued this further. At $x = 1/6$, the O3 ground state is a staged structure with layers of the $x = 1/3$ ordering alternated by vacant layers. Its energy is lowered by 8 meV/CoO_2 if the O3 stacking sequence of the vacant layers is changed to an O1 stacking sequence, thereby producing the globally stable O1-O3 hybrid at $x = 1/6$ (also known as H1-3 [41]). This suggests that there are possible higher order hybrids with the same $x = 1/3$ O3 ordering between vacant O1 layers at even lower compositions, e.g., O1-O1-O3 at $x = 1/9$.

C. P3 orderings

Figure 2(a) shows that the P3 host is stable at intermediate Na concentrations. The two triangular sublattices of Na sites

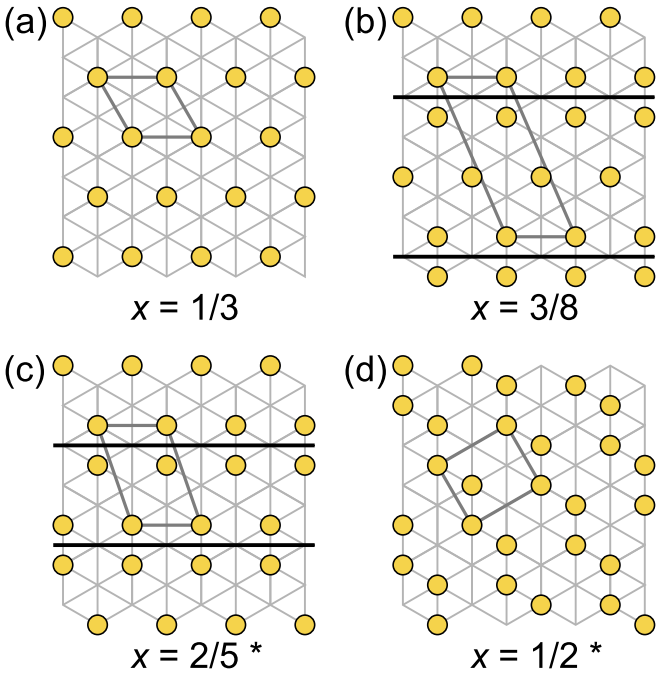

FIG. 5. Orderings on the local convex hull of O3 for $1/3 \leqslant x \leqslant 1/2$. Yellow circles represent Na and black lines indicate APBs between translational variants of the $x = 1/3$ ordering. Unit cells are shown in dark gray. Asterisks indicate that the ordering is above the global hull.

in P3 form a honeycomb network, and we distinguish Na occupancy of the different sublattices with light and dark circles, as in Fig. 6. At $x = 1/2$, the P3 ground state is a zigzag row ordering with Na occupying third-nearest-neighbor sites on the honeycomb network, as shown in Fig. 6a(i). The same ordering has been observed experimentally [50] and predicted computationally [27,48] in several transition-metal oxides and sulfides intercalated with Na. We denote this ordering by ζ, and it forms the foundation of all the hierarchical orderings we identified in P3. We found that the relative stacking of orderings in P3 tends not to affect the energy significantly (within ~2 meV/CoO_2), but we did not test this exhaustively. We also confirmed that occupation of nearest-neighbor sites results in a large energy penalty (>1 eV/Na-Na pair) due to steric repulsion.

We identified three families of hierarchical orderings in P3. Endpoints of these families correspond to important orderings at $x = 1/2$, $x = 4/7$, and $x = 2/3$ [Fig. 6(a)] that we have labeled ζ, η, and Δ, respectively. The Δ ordering can be generated from the η ordering, which itself can be generated from the ζ ordering. This is achieved by introducing different kinds of APBs, which are shown in Fig. 7. We describe each family of orderings next, with naming conventions, composition formulas, and specific ground-state orderings given in the appendix.

1. The ζ^- and ζ^+ orderings in P3

The P3 ground states for $2/5 \leqslant x \leqslant 1/2$ consist of translational variants of ζ separated by APBs, as shown in Fig. 7(a). This type of APB introduces more vacancies compared to

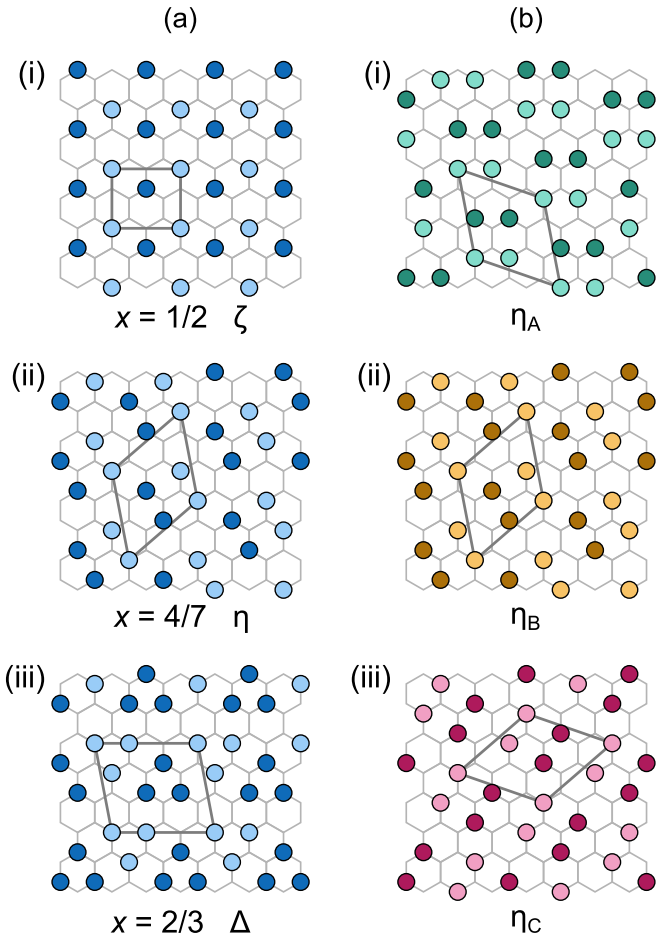

FIG. 6. (a) Important P3 ground-state orderings ζ, η, and Δ, with Na shown in blue. (b) The three orientational variants of the η ordering from (a)(ii), shown in green, orange, and magenta. Unit cells are shown in dark gray. Light and dark circles distinguish Na occupancy of the two distinct triangular sublattices.

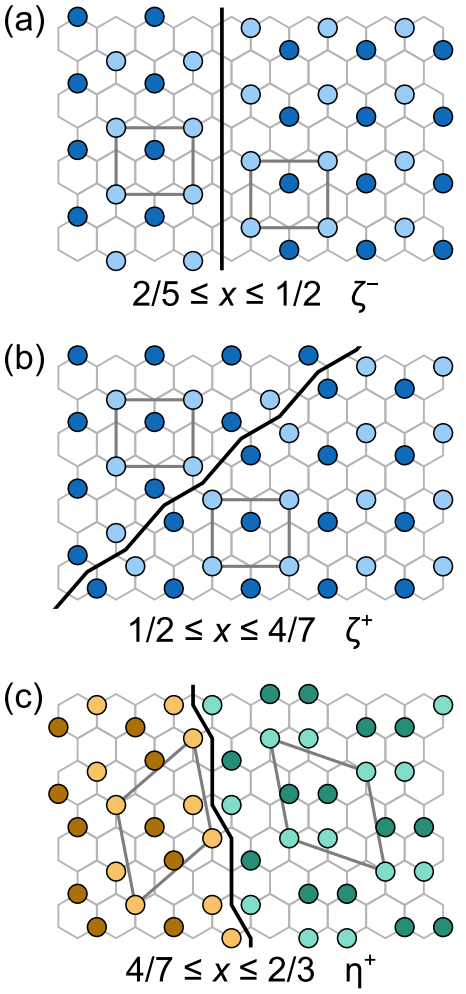

FIG. 7. APBs (black lines) that make up the (a) ζ^-, (b) ζ^+, and (c) η^+ families of hierarchical orderings, separating [(a), (b)] translational variants of the ζ ordering (blue) or (c) orientational variants of the η ordering (orange and green). Unit cells of each variant are shown in dark gray. Light and dark circles distinguish Na occupancy of the two distinct triangular sublattices.

ζ. The infinite possible sequences of APB spacings result in another devil's staircase of hierarchical ground-state orderings. We label this family of orderings as ζ^- and introduce a notation to label them specifically that is similar to that used to describe the θ family (see the Appendix 2, for details).

For $1/2 \leqslant x \leqslant 4/7$, we observe ground states with a different type of APB between translational variants of ζ, as shown in Fig. 7(b). In this type, Na are condensed along the APB, with adjacent third-nearest-neighbor pairs forming quadruplet clusters. As with the ζ^- orderings, one can choose an arbitrarily complex sequence of APB spacings, leading to another family of ground-state orderings which we call ζ^+. Within both the ζ^- and ζ^+ families, multiple structures can have the same composition and are likely degenerate in energy, as discussed in the Appendix 2.

2. The η^+ orderings in P3

The $x = 4/7$ ordering (labeled ζ_4^+) shown in Fig. 6a(ii) is of particular importance and is denoted separately as the η ordering. This is the endpoint of the ζ^+ family, as smaller APB spacings (higher x) do not produce stable orderings. It consists entirely of the quadruplet clusters formed along the ζ^+-type APBs. The η ordering resides in a $\sqrt{7}a \times \sqrt{7}a$ supercell and has three orientational variants η_A, η_B, and η_C related by a threefold rotation, shown as green, orange, and magenta in Fig. 6(b). The three variants are commensurate with the same unit cell, though we have chosen to show the unit cell rotated along with the ordering.

Sections of the two variants η_A and η_B separated by the type of APB shown in Fig. 7(c) form another family of ground-state orderings for $4/7 \leqslant x \leqslant 2/3$, which we refer to as η^+. For a specific naming convention and composition formula, see the Appendix 3. The η^+ orderings are fundamentally different from the ζ^- and ζ^+ orderings in that they alternate between two orientational variants and as such, every η^+ ordering contains an even number of APBs in its unit cell.

Two examples of the η^+ orderings are shown in Fig. 8. The $x = 8/13$ ordering $\eta_{4,4}^+$ consists of equal portions of the two η variants [Fig. 8(a)], while in the $x = 2/3$ ordering, $\eta_{2,4}^+$ or Δ, the η_A regions are half as wide [Fig. 8(b)]. Along the APBs there are triplet clusters of Na on the same triangular

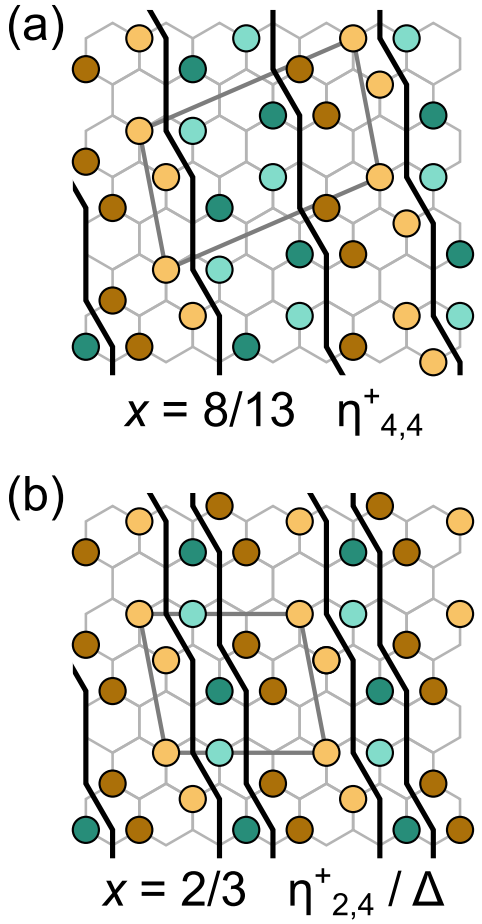

FIG. 8. Example ground-state orderings belonging to the η^+ family in P3, composed of regions of the η_A (green) and η_B (orange) orientational variants separated by APBs (black lines). Unit cells are shown in dark gray. Light and dark circles distinguish Na occupancy of the two distinct triangular sublattices.

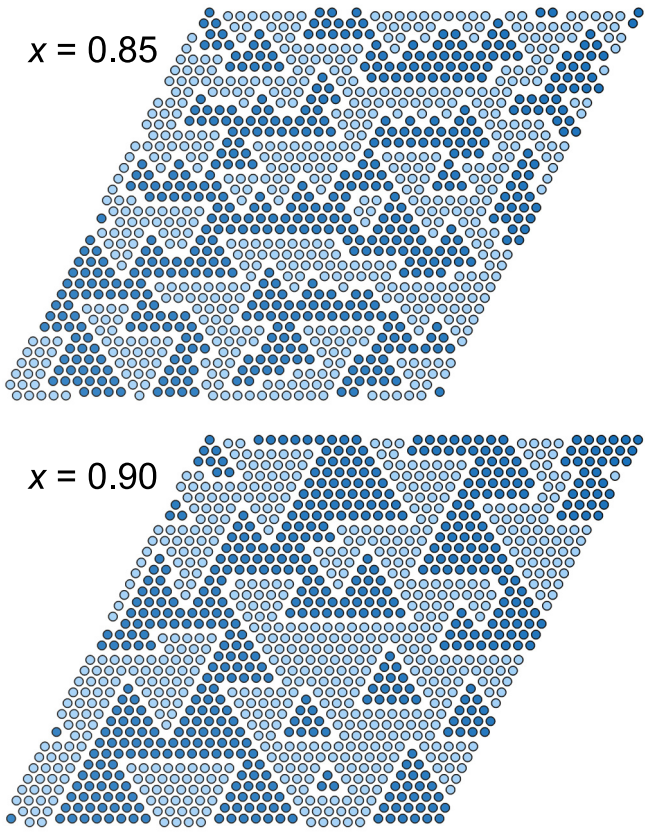

FIG. 9. Representative snapshots from P3 Monte Carlo cooling runs at 300 K (cooled from 1000 K). Light and dark blue circles distinguish Na occupancy of the two distinct triangular sublattices. Visualization created using VESTA [53].

sublattice, shown as light or dark circles, and at $x = 2/3$ the structure is made up entirely of such clusters, as shown in Figs. 6(a)(iii) and 8(b) (note that these are the exact same ordering Δ viewed in different ways).

A hexagonal P3 phase has been reported experimentally around $x = 0.56$, with regions of monoclinic P′3 above and below it in composition [9]. Because $x = 4/7 \approx 0.57$ is close to this composition, we suggest that the experimental phase may correspond to the η ordering, which is described by a hexagonal supercell. Lei *et al.* also speculate that the two regions of P′3 above and below $x = 0.56$ may be distinct ordered superstructures [9], which could correspond to the ζ^+ and η^+ families identified here. In addition to being the endpoint of the η^+ orderings, the Δ ordering at $x = 2/3$ is representative of the low-energy P3 orderings at higher compositions, beyond where P3 is globally stable. These orderings consist of triangular islands of Na on a single sublattice separated by APBs, like those found computationally in Na_xCoO_2 [48,54] and Na_xTiS_2 [27]. Some illustrative snapshots from our Monte Carlo cooling simulations are shown in Fig. 9, with Na on either sublattice indicated with light and dark blue.

IV. DISCUSSION

Our first-principles study of Na_xCoO_2 has revealed several families of stable hierarchical Na orderings that span wide composition ranges. The predicted phase stability follows the experimentally observed O3 → O′3 → P′3 → P3 → P′3 transitions upon deintercalation of $NaCoO_2$, matching both the single-phase composition ranges and the shape of the voltage profile. In addition to the well-known ordering at $x = 1/2$ (ζ), we have identified important orderings in P3 at $x = 4/7$ (η) and $x = 2/3$ (Δ) that may assist experimental studies in resolving structure at these compositions.

We predict a staged hybrid phase for more dilute Na, below compositions that have been accessed experimentally. It is curious that we find a globally stable O1-O3 hybrid at $x = 1/6$ but not a globally stable O1-P3 hybrid at $x = 1/4$, as is the case in Na_xTiS_2 [27]. The O1-P3 hybrid ground state in Na_xTiS_2 consists of layers of the P3 ζ ordering at $x = 1/2$ alternating with vacant O1 layers. Not only does this configuration lie above the common tangent between O3 and O1-O3 for Na_xCoO_2, but it has a higher formation energy than the P3 ground state at $x = 1/4$, which is not staged. This suggests a preference in P3 for Na to spread out within each layer, rather than limiting interlayer interactions by staging.

This study highlights the importance of hierarchical orderings in layered Na intercalation compounds. In each family, orderings consist of regions of favorable local ordering, such

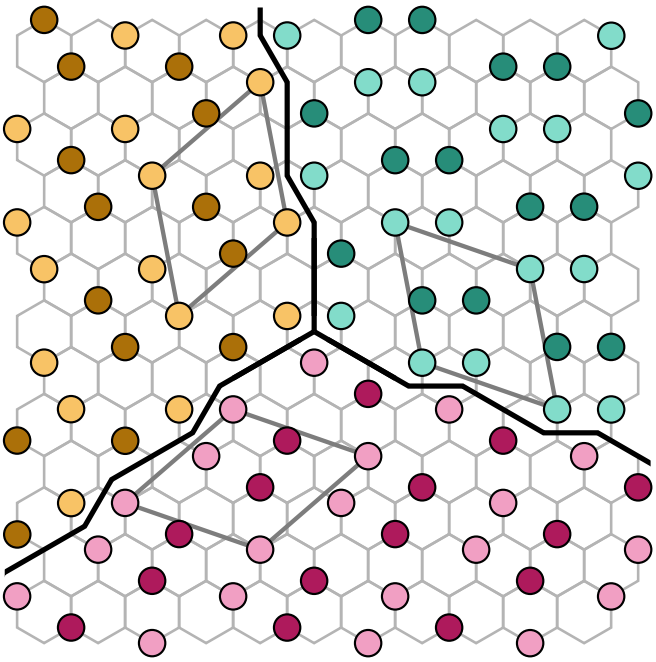

FIG. 10. A hypothetical triple junction between the three orientational variants of the η ordering (green, orange, magenta). Black lines indicate APBs and unit cells of each variant are shown as dark gray boxes. Light and dark circles distinguish Na occupancy of the two distinct triangular sublattices.

as the zigzag rows of the ζ ordering in P3, separated by a particular kind of APB to accommodate changes in composition. Orientational variants occupying the same commensurate supercell offer a convenient way of stitching them together, as is the case with the η ordering. The ordering tendencies described here could lead to even more intricate superstructures. For example, the η ordering could potentially support triple junctions between all three orientational variants separated by the same kind of APB discussed earlier, as illustrated in Fig. 10. We leave the energetics of such structures to be explored in a later study.

Infinite staircases of orderings can be difficult to treat with a cluster expansion approach, as they often require long-range interactions to capture a sufficient number of the ground states. It can also be difficult to find such orderings by brute force enumeration, as even relatively simple hierarchical orderings often require large supercells. Monte Carlo approaches will fail to predict specific orderings if the chosen supercell is not of commensurate shape (even if it is large enough), but may be useful in revealing preferred local ordering phenomena. Also of note is that there is likely a large degeneracy of orderings within a given family. While it is convenient to model simpler ones, experimentally we would expect to see larger superstructrures with different spacings between APBs. Such devil's staircases are common in other types of compounds as well, including metallic alloys [55–57].

The Na ordering of a phase has implications for diffusion and the kinetics of Na insertion and removal. Diffusion in layered intercalation compounds is intimately tied to cation ordering [58–60] and happens differently in P3 compared to O3 [61–63]. Diffusion may occur more readily along APBs, as has been proposed for the orderings of triangular islands for high Na content [27], but likely only along APBs that contain more vacancies compared to the rest of the structure, as in the ζ^- orderings. The insertion and removal of Na in P3 will likely require nonlocal rearrangements of the Na ions. Since the composition of the hierarchical orderings are determined by the density of APBs, any change in composition will require the creation or annihilation of APBs that is simultaneously coupled with a readjustment of the spacing between existing APBs. We leave a detailed examination of these nonlocal diffusion processes for a future study.

Similar families of orderings may be stable in other intercalation compounds that adopt the P3 structure, particularly oxides, where electrostatic effects are strong due to ionicity [26]. This may be the case in alloyed transition-metal oxides like $Na_xFe_{1/2}Co_{1/2}O_2$, which also exhibits the ζ ordering at $x = 1/2$ and undergoes similar structural transformations during cycling [50]. It is possible that the intercalation of K instead of Na may yield the same orderings unless they are somehow destabilized by the larger ionic radius of K^+. Intercalating into different transition-metal oxides like MnO_2 or NiO_2 may see these ordering tendencies competing or coupling with Jahn-Teller distortions, which are critical to understanding the energetics of these systems [64,65]. The Jahn-Teller distortions themselves can take on distinctive orbital orderings within the lattice, such as collinear and zigzag arrangements [66]. The interaction of these with Na orderings is potentially rich but not well explored.

V. CONCLUSION

In this study, we have examined phase stability in Na_xCoO_2 among O3, P3, O1, and staged hybrid structures. The calculated voltage profile agrees qualitatively with experiment. We find that a family of vacancy row orderings are stable in O3 at high Na concentrations, which may correspond to the O′3 phase seen experimentally. At intermediate composition, we have discovered several families of ground-state Na orderings on the honeycomb network in P3 and a unifying picture of their construction. An infinite number of hierarchical orderings are obtained by combining regions of the zigzag row ordering at $x = 1/2$ separated by different types of antiphase boundaries. These orderings are likely to be common among other P3 intercalation compounds.

ACKNOWLEDGMENTS

J.L.K. thanks Julija Vinckevičiūtė and Dr. Maxwell Radin for sharing their valuable insights and Sanjeev Kolli for assisting with structure enumeration. J.L.K. acknowledges support from the U.S. Department of Energy through the Computational Science Graduate Fellowship (DOE CSGF) under Grant No. DE-FG02-97ER25308. This work was supported as part of the Center for Synthetic Control Across Length-scales for Advancing Rechargeables (SCALAR), an Energy Frontier Research Center funded by the U.S. Department of Energy, Office of Science, Basic Energy Sciences under Award No. DE-SC0019381. We acknowledge support from the Center for Scientific Computing from the CNSI, MRL:

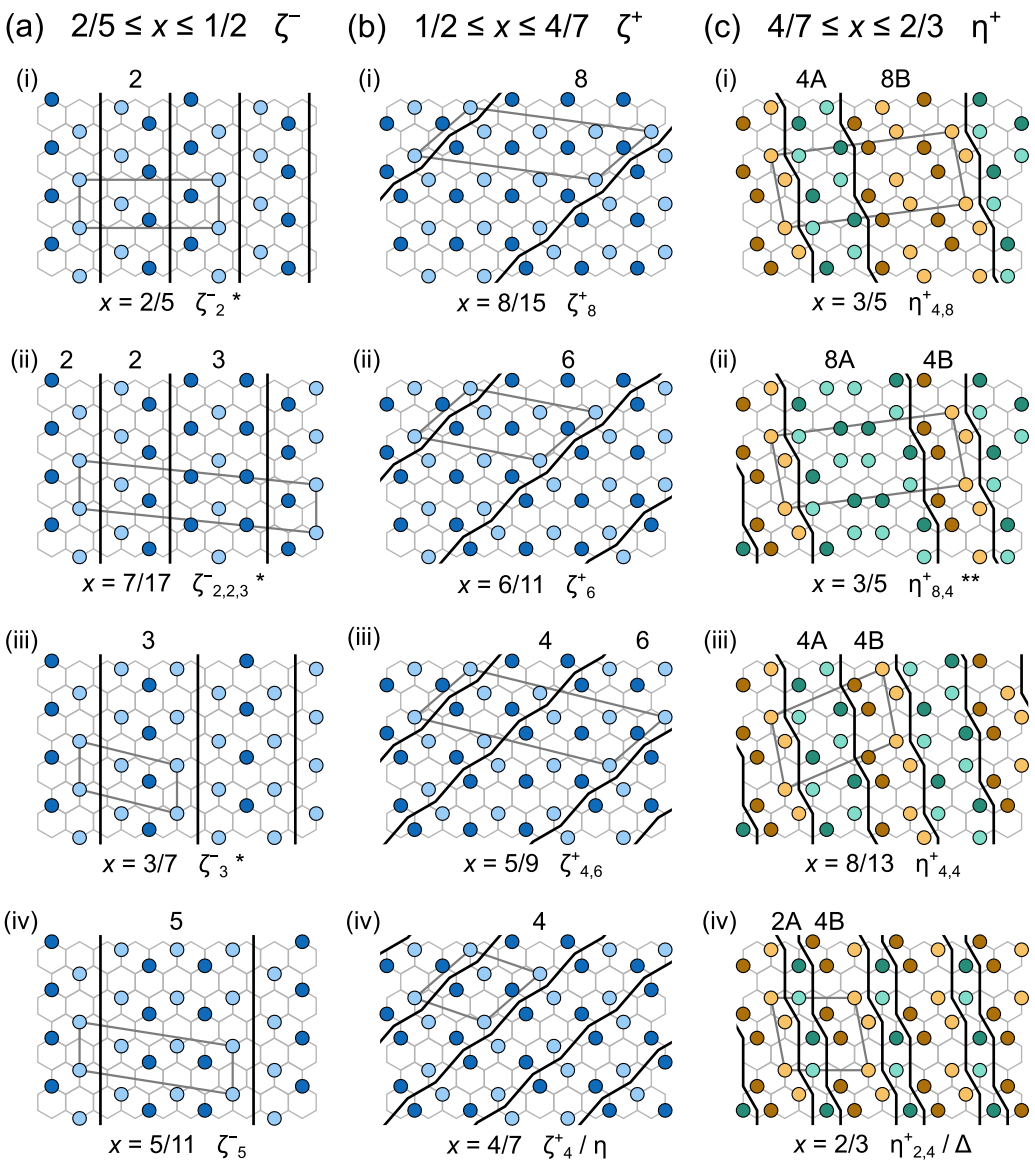

FIG. 11. Orderings belonging to the (a) ζ^-, (b) ζ^+, or (c) η^+ families on or near the local hull of P3. Regions of the ζ ordering are shown in blue, while green and orange represent two orientational variants of the η ordering η_A and η_B, respectively. Light and dark circles distinguish Na occupancy of the two distinct triangular sublattices. Black lines indicate APBs between different [(a), (b)] translational variants of the ζ ordering or (c) orientational variants of the η ordering. Spacings between APBs are indicated above each ordering. Unit cells are shown as dark gray boxes. Single asterisks indicate that the ordering is above the global hull and double asterisks indicate that the ordering is also above the local hull but by less than 2.1 meV/CoO_2.

an NSF MRSEC (DMR-1720256). Computing resources were also provided by the National Energy Research Scientific Computing Center (NERSC), a U.S. Department of Energy Office of Science User Facility operated under Contract No. DE-AC02-05CH11231.

APPENDIX: DETAILS OF HIERARCHICAL ORDERINGS

Here we describe the details of each family of hierarchical orderings in O3 and P3. We define a naming convention for specifying orderings within each family and provide composition formulas. Ground-state orderings belonging to each P3 family are shown in Fig. 11.

1. The θ orderings in O3

The θ orderings in O3 can be viewed as rows of Na periodically separated by rows of vacancies (Fig. 3). We denote a particular row ordering with a tuple S that is appended as a subscript to θ. Each element of the tuple corresponds to the number of filled Na rows between adjacent pairs of vacant rows within the super lattice of the ordering. As an example, consider the $\theta_{4,5}$ ordering shown in Fig. 3(c). In this ordering, four filled Na rows separate one pair of adacent vacant rows, while five filled Na rows separate the next pair of adjacent vacant rows. S for this ordering therefore contains $(4, 5)$. Because of the periodicity of the underlying triangular lattice, S may be reversed or cycled and still describe an equivalent

ordering. The composition of a θ ordering is given by

$$x = \frac{\sum_{k\in S} k}{\sum_{k\in S} (k+1)}, \tag{A1}$$

where k corresponds to the number of filled rows between vacant rows as contained in S. For the $\theta_{4,5}$ ordering, this equation evaluates to

$$x = \frac{4+5}{(4+1)+(5+1)} = \frac{9}{11}. \tag{A2}$$

2. The ζ^- and ζ^+ orderings in P3

The ζ^- and ζ^+ orderings in P3 can both be viewed as regions of translational variants of the ζ ordering [Fig. 6a(i)] periodically separately by one of two kinds of antiphase boundaries (APBs) [Figs. 7(a) and 7(b)]. We introduce a notation for these families that is similar to that used to describe the θ family. The spacing between two APBs is measured by the number of Na atoms in an unbroken zigzag row of the ζ ordering, as shown in Figs. 11(a) and 11(b). We collect the repeated spacings for a given ordering in a tuple S which is used as a subscript in the label. The composition of the ζ^- orderings is then given by

$$x = \frac{\sum_{k\in S} k}{\sum_{k\in S} (2k+1)}, \tag{A3}$$

where k are the individual spacings between APBs contained in S. Note that we have not shown the ζ_4^- ordering at $x = 4/9$ in Fig. 11 because it requires a unit cell of 18 primitive cell volumes, just as the ζ_2^- ordering at $x = 2/5$ requires 10 primitive cell volumes rather than 5. This is because two APBs of this type separated by an even number of Na are not equivalent, as shown in Fig. 11a(i).

For the ζ^+ orderings, we still measure the spacing between APBs by the number of Na atoms in an unbroken zigzag row of the ζ ordering, but spacings are restricted to even values due to the orientation of the APBs [Fig. 11(b)]. The spacings are again collected as a tuple S and used as a subscript. The composition of the ζ^+ orderings is given by

$$x = \frac{\sum_{k\in S} k}{\sum_{k\in S} (2k-1)}. \tag{A4}$$

The composition approaches $x = 1/2$ as the spacings k between APBs go to infinity for both ζ^+ and ζ^-. Multiple sets of spacings can yield the same composition, for example, $\zeta^-_{2,2,4}$ and $\zeta^-_{2,3,3}$ at $x = 8/19$ and ζ^+_8 and $\zeta^+_{6,10}$ at $x = 8/15$. While we did not calculate and compare the energies for any such pair of structures, they would likely be nearly degenerate in energy due to limited interactions between distant APBs.

3. The η^+ orderings in P3

The η^+ orderings in P3 can be viewed as alternating regions of two orientational variants of the η ordering, distinguished by the labels η_A and η_B [Figs. 6(b)(i) and 6(b)(ii)], periodically separately by APBs [Fig. 7(c)]. We present a naming convention for the η^+ family of orderings, similar to that used to describe the ζ^- and ζ^+ orderings. The spacing between two APBs is counted by the number of Na in the unit cell between them belonging to a region of either η_A or η_B, as shown in Fig. 11(c). Because of the geometry of the APBs, the η_B spacings are restricted to multiples of 4 and the η_A spacings are restricted to either 2 or multiples of 4.

We collect the repeated spacings for a given ordering in a tuple S which is used as a subscript in the label. The spacings alternate between the η_A and η_B variants, and we arbitrarily choose that S begin with an η_A spacing. The composition of the η^+ orderings is then given by

$$x = \frac{\sum_{k\in S} k}{\sum_{k\in S} \left(\frac{3}{2}k + \lfloor \frac{k}{4} \rfloor - \frac{1}{2}\right)}, \tag{A5}$$

where k are the individual spacings between APBs contained in S. For the $\eta^+_{4,8}$ and $\eta^+_{8,4}$ orderings, this equation evaluates to

$$x = \frac{4+8}{\left(6+1-\frac{1}{2}\right)+\left(12+2-\frac{1}{2}\right)} = \frac{12}{20} = \frac{3}{5}, \tag{A6}$$

and for the $\eta^+_{2,4}$ ordering, it evaluates to

$$x = \frac{2+4}{\left(3+0-\frac{1}{2}\right)+\left(6+1-\frac{1}{2}\right)} = \frac{6}{9} = \frac{2}{3}. \tag{A7}$$

Figure 11(c) shows ground states belonging to the η^+ family. The orderings $\eta^+_{2,8}$ at $x = 5/8$ and $\eta^+_{4,4,2,4}$ at $x = 7/11$ (not shown) have energies above the hull but by less than 0.5 meV/CoO_2 and are therefore considered as candidate ground states. As with the ζ^+ and ζ^- families, there are several η^+ structures having the same concentration that are essentially degenerate. For example, the two $x = 3/5$ orderings $\eta^+_{4,8}$ and $\eta^+_{8,4}$ shown in Figs. 11(c)(i) and 11(c)(ii) have energies that are within 2 meV/CoO_2 of each other, with the first being on the hull.

Triplet clusters of Na on the same triangular sublattice form along the η^+-type APBs. When APBs are spaced such that the η_A regions are as narrow as possible [$k = 2$, as in the Δ ordering in Fig. 11(c)(iv)], two pairs of Na from adjacent triplet clusters form quadruplet clusters that actually resemble the third orientational variant η_C from Fig. 6(b)(iii).

[1] M. H. Han, E. Gonzalo, G. Singh, and T. Rojo, Energy Environ. Sci. **8**, 81 (2015).

[2] N. Yabuuchi, K. Kubota, M. Dahbi, and S. Komaba, Chem. Rev. **114**, 11636 (2014).

[3] K. Kubota, N. Yabuuchi, H. Yoshida, M. Dahbi, and S. Komaba, MRS Bull. **39**, 416 (2014).

[4] R. Berthelot, D. Carlier, and C. Delmas, Nat. Mater. **10**, 74 (2011).

[5] X. Ma, H. Chen, and G. Ceder, J. Electrochem. Soc. **158**, A1307 (2011).

[6] P. Vassilaras, X. Ma, X. Li, and G. Ceder, J. Electrochem. Soc. **160**, A207 (2012).

[7] M. Guignard, C. Didier, J. Darriet, P. Bordet, E. Elkaïm, and C. Delmas, Nat. Mater. **12**, 74 (2013).
[8] D. H. Lee, J. Xu, and Y. S. Meng, Phys. Chem. Chem. Phys. **15**, 3304 (2013).
[9] Y. Lei, X. Li, L. Liu, and G. Ceder, Chem. Mater. **26**, 5288 (2014).
[10] X. Li, D. Wu, Y. N. Zhou, L. Liu, X. Q. Yang, and G. Ceder, Electrochem. Commun. **49**, 51 (2014).
[11] B. Mortemard de Boisse, D. Carlier, M. Guignard, L. Bourgeois, and C. Delmas, Inorg. Chem. **53**, 11197 (2014).
[12] P. Vassilaras, A. J. Toumar, and G. Ceder, Electrochem. Commun. **38**, 79 (2014).
[13] K. Kubota, I. Ikeuchi, T. Nakayama, C. Takei, N. Yabuuchi, H. Shiiba, M. Nakayama, and S. Komaba, J. Phys. Chem. C **119**, 166 (2015).
[14] H. Liu, J. Xu, C. Ma, and Y. S. Meng, Chem. Commun. **51**, 4693 (2015).
[15] B. Mortemard de Boisse, J. H. Cheng, D. Carlier, M. Guignard, C. J. Pan, S. Bordère, D. Filimonov, C. Drathen, E. Suard, B. J. Hwang *et al.*, J. Mater. Chem. A **3**, 10976 (2015).
[16] D. Wu, X. Li, B. Xu, N. Twu, L. Liu, and G. Ceder, Energy Environ. Sci. **8**, 195 (2015).
[17] C. Didier, M. Guignard, M. R. Suchomel, D. Carlier, J. Darriet, and C. Delmas, Chem. Mater. **28**, 1462 (2016).
[18] M. D. Radin, J. Alvarado, Y. S. Meng, and A. Van der Ven, Nano Lett. **17**, 7789 (2017).
[19] L. Vitoux, M. Guignard, M. R. Suchomel, J. C. Pramudita, N. Sharma, and C. Delmas, Chem. Mater. **29**, 7243 (2017).
[20] C. Delmas, Adv. Energy Mater. **8**, 1703137 (2018).
[21] L. Vitoux, M. Guignard, J. Darriet, and C. Delmas, J. Mater. Chem. A **6**, 14651 (2018).
[22] M. D. Radin, S. Hy, M. Sina, C. Fang, H. Liu, J. Vinckevičiūtė, M. Zhang, M. S. Whittingham, Y. S. Meng, and A. Van der Ven, Adv. Energy Mater. **7**, 1602888 (2017).
[23] T. Wang, D. Su, D. Shanmukaraj, T. Rojo, M. Armand, and G. Wang, Electrochemical Energy Rev. **1**, 200 (2018).
[24] Q. Bai, L. Yang, H. Chen, and Y. Mo, Adv. Energy Mater. **8**, 1702998 (2018).
[25] A. J. Toumar, S. P. Ong, W. D. Richards, S. Dacek, and G. Ceder, Phys. Rev. Appl. **4**, 064002 (2015).
[26] M. D. Radin and A. Van der Ven, Chem. Mater. **28**, 7898 (2016).
[27] J. Vinckevičiūtė, M. D. Radin, and A. Van der Ven, Chem. Mater. **28**, 8640 (2016).
[28] C. Delmas, J.-J. Braconnier, C. Fouassier, and P. Hagenmuller, Solid State Ionics **3–4**, 165 (1981).
[29] G. Kresse and J. Hafner, Phys. Rev. B **47**, 558 (1993).
[30] G. Kresse and J. Hafner, Phys. Rev. B **49**, 14251 (1994).
[31] G. Kresse and J. Furthmüller, Comput. Mater. Sci. **6**, 15 (1996).
[32] G. Kresse and J. Furthmüller, Phys. Rev. B **54**, 11169 (1996).
[33] P. E. Blöchl, Phys. Rev. B **50**, 17953 (1994).
[34] G. Kresse and D. Joubert, Phys. Rev. B **59**, 1758 (1999).
[35] J. Klimeš, D. R. Bowler, and A. Michaelides, J. Phys. Condens. Matter **22**, 022201 (2010).
[36] A. Emly and A. Van der Ven, Inorg. Chem. **54**, 4394 (2015).
[37] M. Aykol, S. Kim, and C. Wolverton, J. Phys. Chem. C **119**, 19053 (2015).
[38] H. Monkhorst and J. Pack, Phys. Rev. B **13**, 5188 (1976).
[39] P. E. Blöchl, O. Jepsen, and O. K. Andersen, Phys. Rev. B **49**, 16223 (1994).
[40] Y. Hinuma, Y. S. Meng, and G. Ceder, Phys. Rev. B **77**, 224111 (2008).
[41] A. Van der Ven, M. K. Aydinol, G. Ceder, G. Kresse, and J. Hafner, Phys. Rev. B **58**, 2975 (1998).
[42] C. Wolverton and A. Zunger, Phys. Rev. Lett. **81**, 606 (1998).
[43] V. L. Chevrier, S. P. Ong, R. Armiento, M. K. Y. Chan, and G. Ceder, Phys. Rev. B **82**, 075122 (2010).
[44] CASM Developers, CASM, version 0.2.X, https://github.com/prisms-center/CASMcode.
[45] J. C. Thomas and A. Van der Ven, Phys. Rev. B **88**, 214111 (2013).
[46] A. Van der Ven, J. C. Thomas, B. Puchala, and A. R. Natarajan, Ann. Rev. Mater. Res. **48**, 27 (2018).
[47] B. Puchala and A. Van der Ven, Phys. Rev. B **88**, 094108 (2013).
[48] Y. Wang, Y. Ding, and J. Ni, J. Phys.: Condens. Matter **21**, 035401 (2009).
[49] See Supplemental Material at http://link.aps.org/supplemental/10.1103/PhysRevMaterials.3.015402 for details about the cluster expansions and Monte Carlo simulations and a link to a database of density functional theory calculations performed in this study.
[50] K. Kubota, T. Asari, H. Yoshida, N. Yaabuuchi, H. Shiiba, M. Nakayama, and S. Komaba, Adv. Funct. Mater. **26**, 6047 (2016).
[51] P. Bak and J. von Boehm, Phys. Rev. B **21**, 5297 (1980).
[52] J. Kanamori, J. Phys. Soc. Jpn. **53**, 250 (1984).
[53] K. Momma and F. Izumi, J. Appl. Crystallogr. **44**, 1272 (2011).
[54] Y. S. Meng, Y. Hinuma, and G. Ceder, J. Chem. Phys. **128**, 104708 (2008).
[55] A. R. Natarajan, E. L. Solomon, B. Puchala, E. A. Marquis, and A. Van der Ven, Acta Mater. **108**, 367 (2016).
[56] E. Decolvenaere, M. J. Gordon, and A. Van der Ven, Phys. Rev. B **92**, 085119 (2015).
[57] J. G. Goiri and A. Van der Ven, Phys. Rev. B **94**, 094111 (2016).
[58] A. Van der Ven, G. Ceder, M. Asta, and P. D. Tepesch, Phys. Rev. B **64**, 184307 (2001).
[59] A. Van der Ven, J. C. Thomas, Q. Xu, B. Swoboda, and D. Morgan, Phys. Rev. B **78**, 104306 (2008).
[60] A. Van der Ven, J. Bhattacharya, and A. A. Belak, Acc. Chem. Res. **46**, 1216 (2013).
[61] T. Shibata, Y. Fukuzumi, W. Kobayashi, and Y. Moritomo, Sci. Rep. **5**, 9006 (2015).
[62] S. Guo, Y. Sun, J. Yi, K. Zhu, P. Liu, Y. Zhu, G. Z. Zhu, M. Chen, M. Ishida, and H. Zhou, NPG Asia Mater. **8**, e266 (2016).
[63] T. J. Willis, D. G. Porter, D. J. Voneshen, S. Uthayakumar, F. Demmel, M. J. Gutmann, M. Roger, K. Refson, and J. P. Goff, Sci. Rep. **8**, 3210 (2018).
[64] M. E. Arroyo y de Dompablo, C. Marianetti, A. Van der Ven, and G. Ceder, Phys. Rev. B **63**, 144107 (2001).
[65] X. Li, X. Ma, D. Su, L. Liu, R. Chisnell, S. P. Ong, H. Chen, A. Toumar, J. C. Idrobo, Y. Lei *et al.*, Nat. Mater. **13**, 586 (2014).
[66] M. D. Radin and A. Van der Ven, Chem. Mater. **30**, 607 (2018).